Korean J. Chem. Eng., 39(4), 876-886 (2022)
DOI: 10.1007/s11814-021-0971-5

pISSN: 0256-1115
eISSN: 1975-7220

Study on the performance of different discharging devices of a continuous production system

Zhenya Duan*, **Jie Wang***, **Shujie Sun***, **Wenchen Li***, **Haodong Zhang***,
Guoyue Qiao*, **Junmei Zhang**,†**, and **Jingtao Wang*****

*College of Electromechanical Engineering, Qingdao University of Science and Technology, Qingdao 266061, China
**College of Chemical Engineering, Qingdao University of Science and Technology, Qingdao 266042, China
***School of Chemical Engineering and Technology, Tianjin University, Tianjin 300072, China

(*Received 27 January 2021 • Revised 25 August 2021 • Accepted 29 September 2021*)

Abstract−Based on the developed continuous production system of sodium phenol carboxylation reaction, several types of discharging devices are proposed, which are suitable for the case where the transported particles are not easy to maintain a stable state in the transported fluid. Numerical simulations of the gas-solid two-phase flow characteristics and particle distribution were performed with DPM, and the particle retention ratio and fluid loss degree were proposed to investigate the performance of the discharging devices. The results of simulations and industrial experiments showed that a guide plate installed in the "B" discharging device can solve the accumulation problem, realize the efficient and continuous delivery of the particles, and maintain a uniform distribution of particles. This study can provide a reference for the design of a gas-solid two-phase discharging device, and guide the industrial experimental operation and modification of continuous production systems for sodium phenol carboxylation.

Keywords: Continuous Production, Numerical Simulation, Gas-solid Two-phase Flow, Particle Distribution, Discharging Device

INTRODUCTION

Continuous production is a developmental trend of the chemical and pharmaceutical industries that can effectively simplify the steps of the production process, realize the strengthening of the reaction process, reduce energy consumption, and further improve the level of automation and informationization of production. Wide use in petrochemical, pharmaceutical, and other fields involving fluidized beds can achieve full contact and reaction between phases, with good heat and mass transfer and mixing effect, for the realization of chemical production of continuous process transformation has a high adaptability [1,2]. Sodium phenol carboxylation to generate sodium salicylate is an important step in the production of salicylic acid (a precursor for the preparation of aspirin), which uses batch production presently. Our team has been conducting long-term in-depth research on the reaction process conditions, mechanism, and reaction kinetics of sodium phenol carboxylation, and proposed a continuous production system of salicylic acid production intermediates, in which a fluidized bed is the main reaction equipment [3]. Spray drying technology is used to prepare low moisture content sodium phenol particles with an average particle size of 50 μm, class A particles [4], with good flowability index, which are delivered to the designated storage tank with inert gas. Then, the sodium phenol particles are transported to the fluidized bed using carbon dioxide gas through the discharging device. The particles react with the CO_2 under ideal conditions to produce solid sodium salicylate and achieve continuous operation of the process.

Pneumatic conveying is a method of conveying powdery and granular materials in pipelines using gas flow as conveying power, which has the advantages of a closed system, flexible pipeline arrangement, high efficiency, easy maintenance, and operation. It is widely used in the gas-solid two-phase flow process [5-7]. In the above continuous production process transformation, the pneumatic conveying system is mainly used as a discharging device for the fluidized bed front-end process. The strength of its conveying capacity directly affects the flow state and reaction characteristics of the particles in the fluidized bed, which requires the pneumatic conveying system to have good transport characteristics to efficiently transport sodium phenol particles into the fluidized bed and provide a guarantee for the continuous production of such reaction.

Compared to other types of conveying methods, pneumatic conveying exhibits higher efficiency and less impact on particle quality. Yet, the design of an efficient pneumatic conveying is a challenge. Small changes in the device or product can cause changes in conveying performance. A number of studies using computational fluid dynamics (CFD) have reported the effects of particle parameters such as sphericity, particle size, particle-wall interaction, and particle-wall adhesion, solid to gas ratio, pressure distribution characteristics, and pressure drop changes on the fluid dynamics of pneumatic conveying device [8-14], which are important factors in the fluidization construction of pneumatic conveying devices. Liu et al. [15] analyzed the effect of particle collision conditions on the pressure loss in transport pipelines by simulation and concluded that particle collision can reduce the pressure loss and promote the homogenization of dynamic pressure distribution in the outlet section, which is conducive to improving pipeline conveying efficiency. But

---

†To whom correspondence should be addressed.
E-mail: qust_zyduan@163.com

there is a lack of an accurate characterization method for the pressure loss, and the simulation results lack experimental verification. To understand the flow mechanism of pneumatic conveying in segment plug flow, Orozovic et al. [16] integrated a large amount of literature and data to predict the characteristic constants in segment plug flow and proposed to establish data relations for predicting equivalent steady-state conditions for segment plugs. But this prediction still needs the assistance of other equations and the prediction accuracy cannot be guaranteed due to the reliability problem of the data. The latest research delves into more detailed areas. Wang [17] found that vortices and refluxes occur in the core region of the jet under the effect of high speed air curl suction, and concluded that normal and spreading vortices promote the mixing between two phases, accelerate the process of momentum and energy transfer between phases; the flow vortices mainly play the role of driving the material movement. The collision and adhesion of micron-sized particles with the wall play a decisive role in the particle deposition process, for which Hong et al. [18] investigated the deposition behavior of fine particles on rough walls and found that turbulent kinetic energy is stronger in the rough wall region compared to the smooth region, leading to an increase of 1-2 orders of magnitude in the deposition rate of small particles. Sharma et al. [19] developed a new particle velocity model which shows that the particle slip velocity decreases with increasing air mass flow. There are also scholars who conducted acoustic analysis of particle-wall interaction in segmental plug flow, established an acoustic model, and introduced machine learning to improve the accuracy of acoustic emission detection [20,21]. Although these studies are at the forefront of theory, the reliability needs to be further evaluated and the degree of application in practical production is yet to be tested.

In addition, the current pneumatic conveying device has various structural styles, such as bent tube discharging device, venturi feeder, and screw feeder. And the flow of powder inside it is also very complicated, with its discharging process involving many practical problems, such as clogging and accumulation, poor discharging, and bridging, which seriously affects the system operation. Many studies have been made to address these problems. Xiong et al. [22] investigated the blockage problem for dense phase pneumatic conveying of pulverized coal in horizontal pipes, and by profiling the characteristic information of the pressure signal, they deduced the relationship between the critical velocity of blockage and the inner diameter of the pipe and the nature of the carrier gas and established criteria, but there was a lack of connection between the operating conditions and the structure. Zhou et al. [23] evaluated the efficiency and stability of cyclone pneumatic conveying by static pressure loss and pressure fluctuation difference with good accuracy, and concluded that cyclonic flow has better energy saving performance and conveying performance; however, the study was conducted for lumpy larger particles, and the reliability for spherical fine particles needs to be further explored. Bansal et al. [24] explored the conveying characteristics of pneumatic conveying fluidization in a straight pipe with fine powder, and found that fine powder fluidized conveying has a high pipe dependence. In fact, in practical engineering due to the constraints of site conditions, some complex devices are difficult to use, and the complex piping can make particle flow characteristics more difficult to grasp, so bends are often used for conveying, but unstable flow is easily formed in bends, resulting in adverse effects such as phase separation, pipeline vibration, wall wear, pipe buildup, and increased pressure drop (increased kinetic energy demand for conveying) [25-27]. In this case, it is significant to develop a new type of pneumatic conveying discharging device for the actual project and avoid the related problems at the same time.

In this paper, for the continuous production system of sodium phenol carboxylation, different structures of pneumatic conveying discharging devices were designed and developed. Combined with the discrete particle model (DPM), numerical simulations were used to investigate the flow characteristics of gas-solid two-phase flow and particle distribution characteristics in two different forms of discharging devices. And the reliability of the numerical simulations was verified experimentally. Further, based on the results of the study, the discharging device was improved, and the particle retention ratio and the fluid loss degree were proposed to quantitatively examine the performance of the new discharging device. The analysis concluded that the new discharging device has high efficiency and continuous conveying capability. This study can provide a reference for the design of a gas-solid two-phase flow conveying device, and provide effective guidance for the optimization of the continuous production process and experimental operation of similar reactions.

MATHEMATICAL MODELS

1. Physical Conservation Law Control Equations

The gas-solid two-phase flow obeys the laws of conservation of physics, mainly including the law of conservation of mass, the law of conservation of momentum, and the control equation is a mathematical description of these conservation laws.

Conservation of mass equation:

$$\frac{\partial(\alpha_g\rho_g)}{\partial \mathrm{t}}+\frac{\partial(\alpha_g\rho_g\mathrm{u}_x)}{\partial \mathrm{x}}+\frac{\partial(\alpha_g\rho_g\mathrm{u}_y)}{\partial \mathrm{y}}=0 \tag{1}$$

Conservation of momentum equations:

$$\begin{aligned}&\frac{\partial(\alpha_g\rho_g\mathrm{u}_x)}{\partial \mathrm{t}}+\frac{\partial(\alpha_g\rho_g\mathrm{u}_x\mathrm{u}_x)}{\partial \mathrm{x}}+\frac{\partial(\alpha_g\rho_g\mathrm{u}_y\mathrm{u}_x)}{\partial \mathrm{y}}\\&=\frac{\partial}{\partial \mathrm{x}}\left(\alpha_g(\mu_g+\mu_t)\frac{\partial \mathrm{u}_x}{\partial \mathrm{x}}\right)+\frac{\partial}{\partial \mathrm{y}}\left(\alpha_g(\mu_g+\mu_t)\frac{\partial \mathrm{u}_x}{\partial \mathrm{y}}\right)-\alpha_g\mathrm{S}_x+\mathrm{F}_{p,\,x}\end{aligned} \tag{2}$$

and

$$\begin{aligned}&\frac{\partial(\alpha_g\rho_g\mathrm{u}_y)}{\partial \mathrm{t}}+\frac{\partial(\alpha_g\rho_g\mathrm{u}_x\mathrm{u}_y)}{\partial \mathrm{x}}+\frac{\partial(\alpha_g\rho_g\mathrm{u}_y\mathrm{u}_y)}{\partial \mathrm{y}}\\&=\frac{\partial}{\partial \mathrm{x}}\left(\alpha_g(\mu_g+\mu_t)\frac{\partial \mathrm{u}_y}{\partial \mathrm{x}}\right)+\frac{\partial}{\partial \mathrm{y}}\left(\alpha_g(\mu_g+\mu_t)\frac{\partial \mathrm{u}_y}{\partial \mathrm{y}}\right)-\alpha_g\mathrm{S}_y+\mathrm{F}_{p,\,y}\end{aligned} \tag{3}$$

where,

$$\mathrm{S}_x=-\frac{\partial \mathrm{p}}{\partial \mathrm{x}}+\frac{\partial}{\partial \mathrm{x}}\left((\mu_g+\mu_t)\frac{\partial \mathrm{u}_x}{\partial \mathrm{x}}\right)+\frac{\partial}{\partial \mathrm{y}}\left((\mu_g+\mu_t)\frac{\partial \mathrm{u}_y}{\partial \mathrm{x}}\right) \tag{4}$$

$$\mathrm{S}_y=-\frac{\partial \mathrm{p}}{\partial \mathrm{y}}+\frac{\partial}{\partial \mathrm{x}}\left((\mu_g+\mu_t)\frac{\partial \mathrm{u}_x}{\partial \mathrm{y}}\right)+\frac{\partial}{\partial \mathrm{y}}\left((\mu_g+\mu_t)\frac{\partial \mathrm{u}_y}{\partial \mathrm{y}}\right)+\rho_g\mathrm{g} \tag{5}$$

2. Numerical Simulation Models

Numerical simulations are implemented with the DPM model, which uses the Euler-Lagrange method to describe the gas phase by Euler and the particle phase by Lagrange. In this study, the particle phase is treated by the theoretical model of particle dynamics, in which the interaction between gas and solid is calculated by the Stokes-Cunningham drag equation, and the gas phase is treated by the SST k-ω turbulence model.

2-1. Particle Dynamics Models

In the discrete phase model calculations, the trajectory of the particle phase is traced using Lagrangian coordinates. The equation of equilibrium of forces acting on the particles (particle inertia= various forces acting on the particles) in the Cartesian coordinate system has the following form (x-direction):

$$\frac{du_s}{dt}=F_D(u_g-u_s)+\frac{g_x(\rho_s-\rho_g)}{\rho_s}+F_x \tag{6}$$

For particle motions with small diameters, the Stokes-Cunningham drag equation is applicable. In this case, the F_D equation is shown in Eq. (7).

$$F_D=\frac{18\mu}{d_s^2\rho_s C_C} \tag{7}$$

The coefficient C_C in the above equation is the Cunningham correction of the Stokes drag equation (correction for particle wall velocity slip considering dilute gas mechanics), which is calculated as

$$C_C=1+\frac{2\lambda}{d_s}\left(1.257+0.4e^{-(1.1d_s/2\lambda)}\right) \tag{8}$$

2-2. The SST k-ω Model

The SST k-ω model is a variation of the standard k-ω model, combining the k-ω in free flow and the k-ω model close to the wall. It does not use the wall function and requires higher boundary layer mesh accuracy, has high computational accuracy for the flow-solid separation at the wall, and can obtain the sidewall flow well, which is most accurate when solving the flow near the wall. Therefore, the SST k-ω model was used as a turbulence model for this simulation.

The SST k-ω model includes two equations for the transport of the specific turbulent kinetic energy k and the specific turbulent dissipation rate ω, respectively.

$$\frac{\partial}{\partial t}(\rho_g k)+\frac{\partial}{\partial x_i}(\rho_g k u_i)=\frac{\partial}{\partial x_j}\left(\mu_k\frac{\partial k}{\partial x_j}\right)+G_k-Y_k+S_k \tag{9}$$

and

$$\frac{\partial}{\partial t}(\rho_g\omega)+\frac{\partial}{\partial x_i}(\rho_g\omega u_i)=\frac{\partial}{\partial x_j}\left(\mu_\omega\frac{\partial\omega}{\partial x_j}\right)+G_\omega-Y_\omega+D_\omega+S_\omega \tag{10}$$

where the effective viscosity is given by the following equations:

$$\mu_k=\mu+\mu_t\frac{1}{\sigma_k} \tag{11}$$

$$\mu_\omega=\mu+\mu_t\frac{1}{\sigma_\omega} \tag{12}$$

where, μ_t is the turbulent viscosity used to accurately capture the onset of separation under a pressure gradient, given by the following equation:

$$\mu_t=\frac{\rho_g k}{\omega}\frac{1}{\max\left[\frac{1}{\alpha^*},\frac{SF_2}{a_1\omega}\right]} \tag{13}$$

where,

$$F_2=\tanh(\Phi_2^2) \tag{14}$$

$$\Phi_2=\max\left[2\frac{\sqrt{k}}{0.09\omega y},\frac{500\mu}{\rho_g y^2\omega}\right] \tag{15}$$

SIMULATION SETTINGS

1. Geometric Models and Meshing

We initially designed and manufactured two different types of discharging devices, defined separately as the "A" discharging device and the "B" discharging device. We added an inclined guide plate to the "B" discharging device. Fig. 1 shows the fluid area geometry models and meshes divisions for the three discharging devices, where the geometry models were created by UG NX 10.0, and the fluid calculation area dimensions are the same as the actual dimensions. The origin of the coordinate system is arranged at the center of the inlet pipe above the discharging device. The mesh is divided by FLUENT Meshing, all poly meshes are used, the maximum distortion rate is less than 0.4, and the maximum growth rate of the adjacent mesh is 1.2. Controlling the number of meshes by setting their size, and applying the same simulation method and boundary conditions for models with different numbers of meshes, for

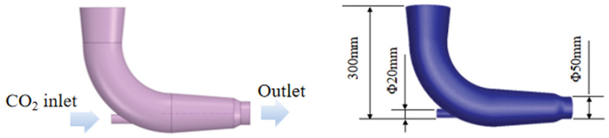

"A" discharging device

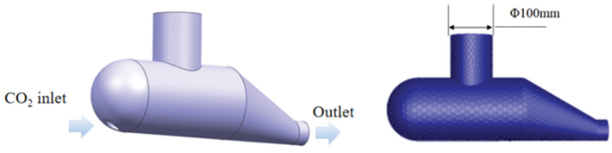

"B" discharging device

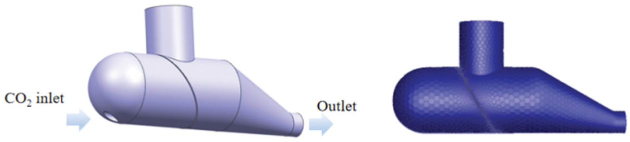

"B" discharging device(installed guide plate)

Fig. 1. Geometric model and grid division of several discharging devices.

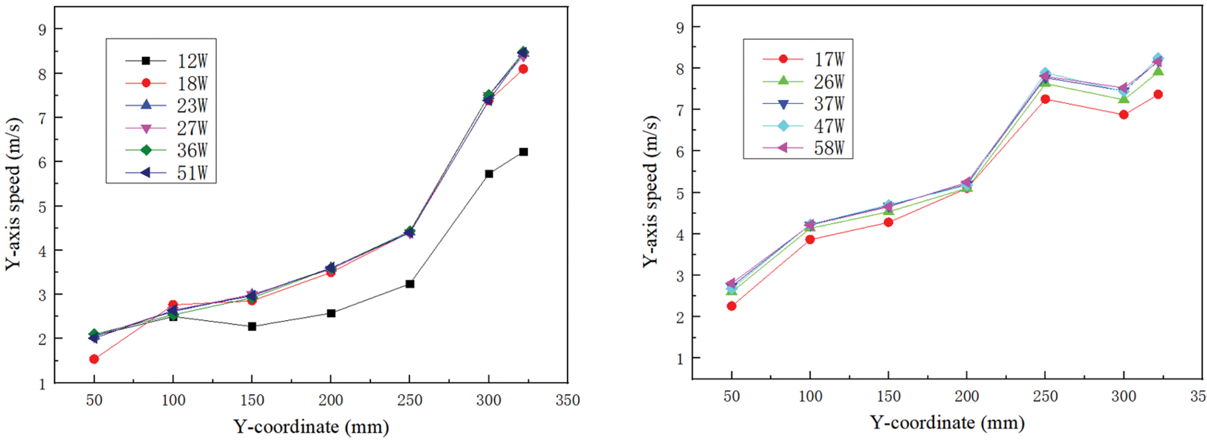

(a) "A" discharging device (b) "B" discharging device

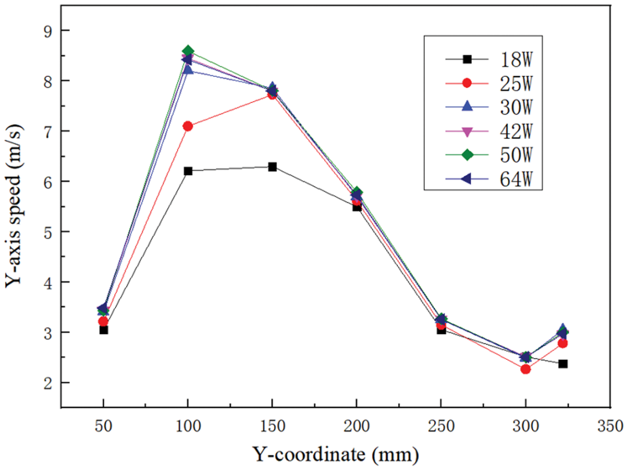

(c) "B" discharging device (installed guide plate)

Fig. 2. Gas Y-axis velocities at different coordinates along the exit center normal.

Table 1. Parameters and properties' set in simulation

Gas-phase	Settings	Solid-phase	Settings
Turbulence model	SST K-Omega	Gas-solid coupling	DPM
Gas-phase	CO_2	Particle time step (s)	0.001
Gas-phase time step (s)	0.01	Particles diameter (m)	5×10^{-5}
Gas-phase inlet direction	x: 0, y: 1, z: 0	Solid-phase density (kg/m^3)	890
Gas-phase density (kg/m^3)	13	Normal coefficient of restitution	0.8
Outlet gas pressure (MPa)	0.6		
Gas-phase inlet velocity (m/s)	17.7		

monitoring of the gas Y-axis velocity on the center normal line (x=0, z=−225 mm) at the outlet of discharging devices, the results are shown in Fig. 2. Considering the accuracy and the amount of calculation of the simulation, we chose the mesh number of model of 230 thousand for the A discharging device, 370 thousand for the B discharging device, and 420 thousand for the B discharging device (installed guide plate).

2. Simulation Codes and Numerical Algorithms

The gas-phase flow field is calculated in "Steady" in Ansys Fluent 16.0. The SIMPLE algorithm is applied for pressure-velocity coupling, and the relationship between pressure correction and velocity is exploited to achieve mass conservation and thus the pressure field. After the convergence of the continuous phase in "Steady", particles were injected using the DPM method and adjusting the algorithm to "Coupled" and the arithmetic procedure to "Transient". We investigated the effect of different solid mass flow rates (0.1 kg/s, 0.2 kg/s, and 0.3 kg/s) on the particle distribution and flow state in different discharging devices. The parameter settings of the simulation process are shown in Table 1. The gas-solid two-phase flow inside the discharging device for 100 s was examined to obtain suffi-

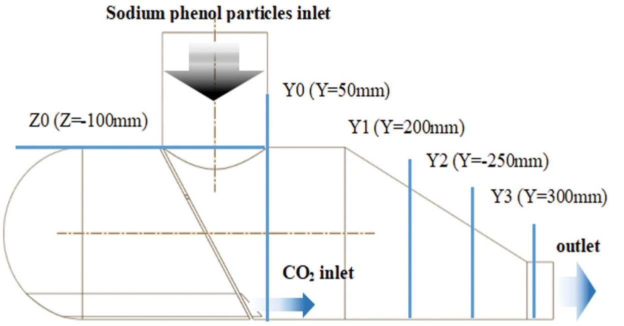

Fig. 3. Boundary condition setting (example of B discharging device installed guide plate).

ciently reliable data for comparison with the experimental values.

3. Calculation Methods and Boundary Conditions

Gas velocity was specified at the gas-phase inlet, with a positive velocity direction along the Y-axis and the discrete phase was set to “Reflect”. The outlet was set to “Pressure Outlet” and the discrete phase was set to “Escape”. The boundary condition settings are shown in Fig. 3. The gas phase is a non-slip boundary condition along the wall, and the interaction between the particles and the wall is achieved by the coefficient of restitution, and the specific simulation parameters are listed in Table 1.

EXPERIMENTAL SETUP

The discharging system shown in Fig. 4 consists of a sodium phenol storage tank, kick-out device, discharging device, gas supply line, gas and solids delivery line. During the experiment, the solid mass flow rate was determined by the speed of the kick-out device: at 20% speed, the particle mass flow rate was 0.1 kg/s; at 40% speed, it was 0.2 kg/s; at 60% speed, it was 0.3 kg/s. The pressure of the sodium phenol storage tank was maintained by the gas supply line. And there were flow and pressure gauges installed on both the gas supply line and the gas delivery line, and the gas delivery flow rate was mainly controlled by valves and gas sources.

Experimental data collection: as mentioned before, there are flow and pressure gauges installed on the delivery line, among which the field flow instruments (FI) are set on the gas delivery line for gas flow data collection, the pressure gauges (PG) are set on the gas delivery line before and after the discharging device for pressure data collection, and the material flow data collection by converting the speed of the kick-out device to material flow. The flow meters, the speed of the kick-out device, and pressure gauges are connected to the central control platform for direct control and reading of the values.

RESULTS AND DISCUSSION

1. Model Validation

Fig. 5 shows the differential pressure of the different sections relative to the outlet of discharging devices A and B. In the experiment, the differential pressure was obtained by pressure gauges mounted on the storage tank, front of the gas phase inlet, and the outlet. In the simulation, in order to characterize the pressure variation along with the discharging device in more detail, five cross-sections were created: Z0 (Z=−100 mm), Y0 (Y=50 mm), Y1 (Y=200 mm), Y2 (Y=250 mm) and Y3 (Y=300 mm). The experimental and simulated values are shown in Fig. 3. Both experiments and simulations were run at a stable particle mass flow rate of 0.1 kg/s; then we took the average of the results over 20 s-100 s. As shown in Fig. 5, the experimental values obtained from the same discharging device are slightly larger than the simulated values, which may be due to the large volume of the storage tank; the pressure gauge is difficult to obtain the pressure of the specified cross-section accurately. On the whole, the error between the simulation results and the experimental value is not more than 7%, so the simulation method is feasible.

No matter experimental or simulation, the pressure difference between the import and export of the B discharging device is larger than that of the A discharging device, and the B discharging device

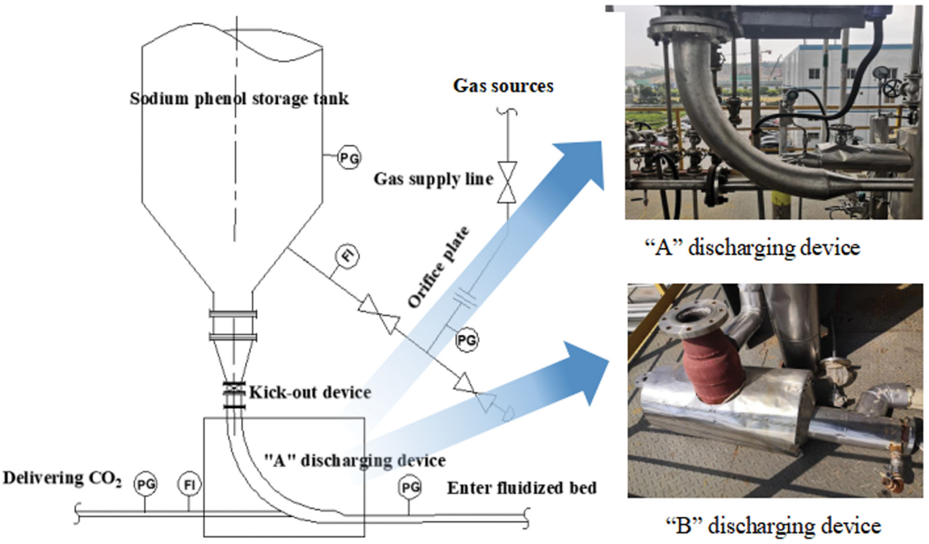

Fig. 4. Discharging devices and the experimental procedure.

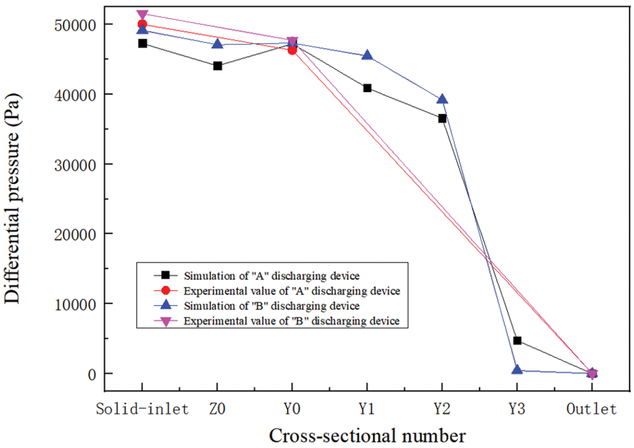

Fig. 5. Difference in time average pressure between the cross-section and the outlet of A and B discharging device at 0.1 kg/s.

has a larger contraction section before the exit, so the pressure drop in this area is faster than that of the A discharging device, and the faster pressure drop can make the gas carry-out ability stronger; the pressure distribution cloud diagram is shown in Fig. 6. In contrast, the pressure distribution of CO_2 gas in the chamber is more uniform in the B discharging device, and the uniform fluid distribution will reduce the disturbance factor of the airflow field and help the particles flow more smoothly with the gas.

2. Gas-solid Two-phase Flow

Fig. 7 is vector diagrams of the gas velocities in discharging devices A and B. It can be seen that the mass flow rate of solids inlet does not have a significant effect on the gas flow in the discharging device. The gas flow is smoother in the main part of the A discharging device, but in the B discharging device, the left side of the vertical discharging tube is on the back side of the particle inlet and the gas inlet, which makes some of the gas flow back and forms a "reflux chamber", which can lead to prolonged stagnation of the particles.

Fig. 8 shows a cloud plot of the time average solids content at different mass flow rates in the discharging device A and B. The particle accumulation area at the lower end of the A discharging device becomes larger as the mass flow rate increases. This is because a "high-speed zone" is formed in the middle of the inlet and a blind zone outside the "high-speed zone" after the gas enters the discharging device from the gas phase inlet, which makes it hard for the particles to leave the blind zone. At a particle mass flow of 0.2 or 0.3 kg/s, the zone of particle accumulation extends all the way to the solids outlet. And this is consistent with the regional heat phenomena observed during the experiment. Compared to the A discharging device, the B discharging device does not show a more severe accumulation at the front end of the gas inlet, because the gas cyclone occurs here in the B discharging device, and the suitable size of the cyclone can disturb the particles deposited at the bottom of the pipe and increase the particle velocity to improve the transport performance. However, as mentioned, particle aggregation along the wall does occur in the "reflux chamber" at the back end of the gas inlet, and the thickness of the particle aggregation increases with increasing mass flow rate.

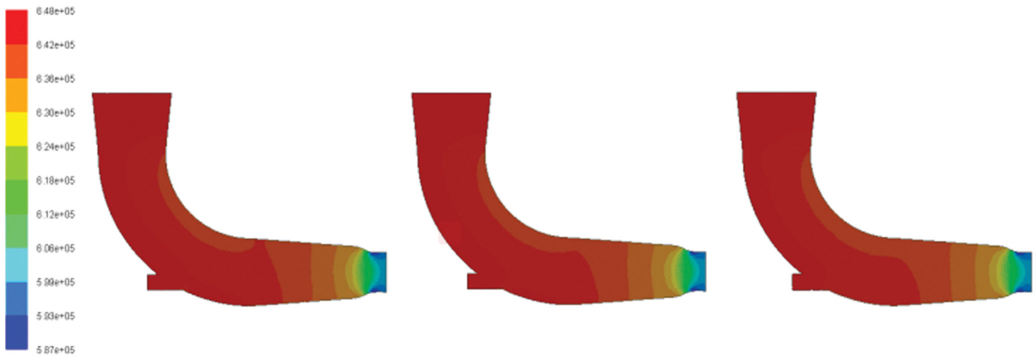

(a) "A" discharging device

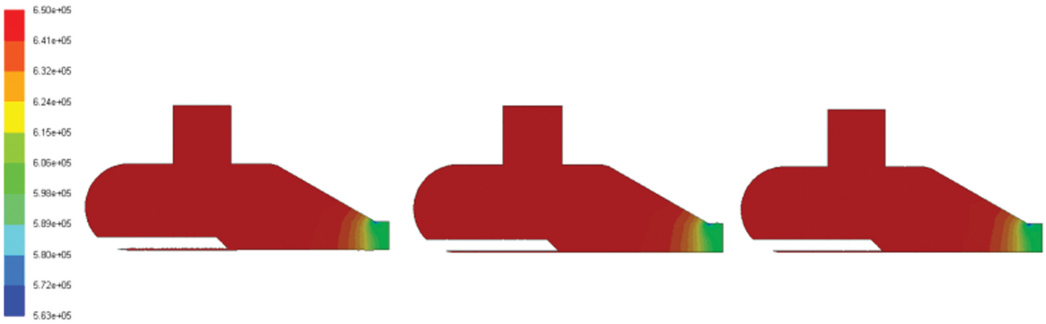

(b) "B" discharging device

Fig. 6. Pressure distribution of A and B discharging devices at X=0 cross-section.

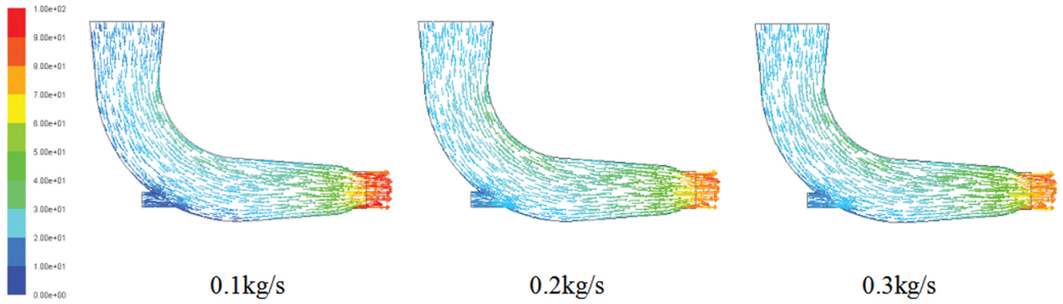

(a) “A” discharging device

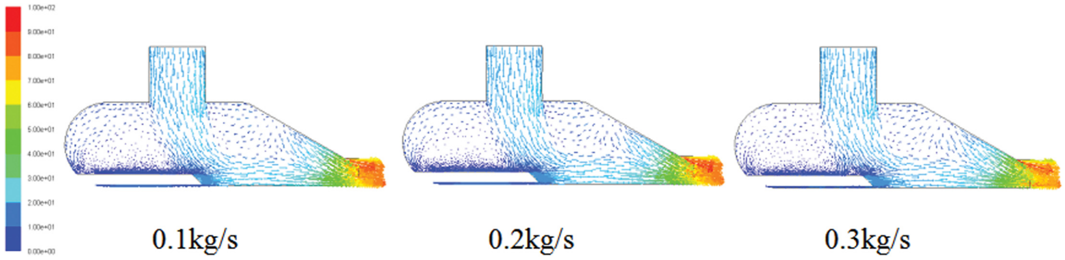

(b) “B” discharging device

Fig. 7. Gas velocity vector for the X=0 mm cross-section of discharging devices A and B.

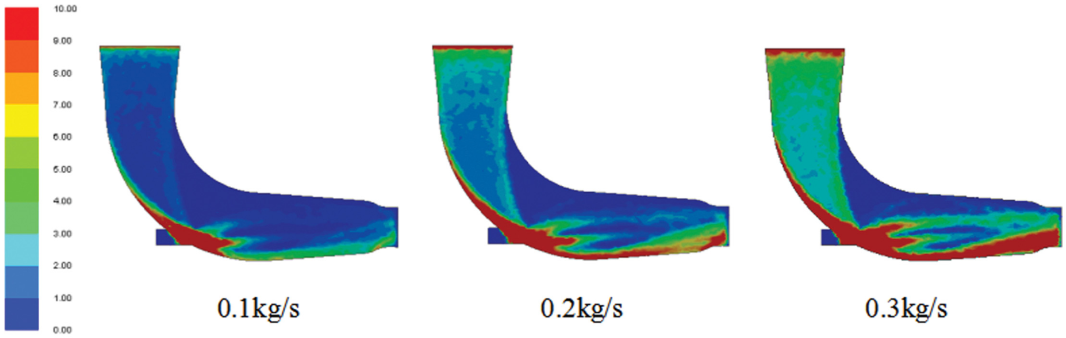

(a) “A” discharging device

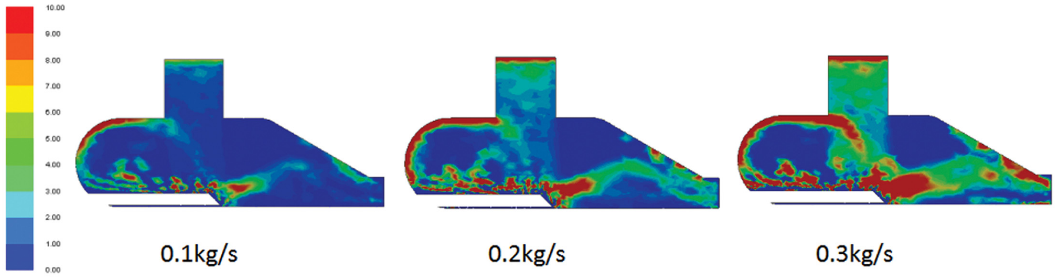

(b) “B” discharging device

Fig. 8. Solids content distribution at X=0 mm cross-section.

3. Improvement and Optimization of the B Discharging Device (Installed Guide Plate)

In contrast, the B discharging device had a more uniform pressure distribution and no significant particle accumulation. But it needed to be modified to improve the gas reflux and particle aggregation that occurs at the back end of the gas inlet. We installed a guide plate in the B discharging device, which became a new structure of discharging device, as shown in Fig. 3.

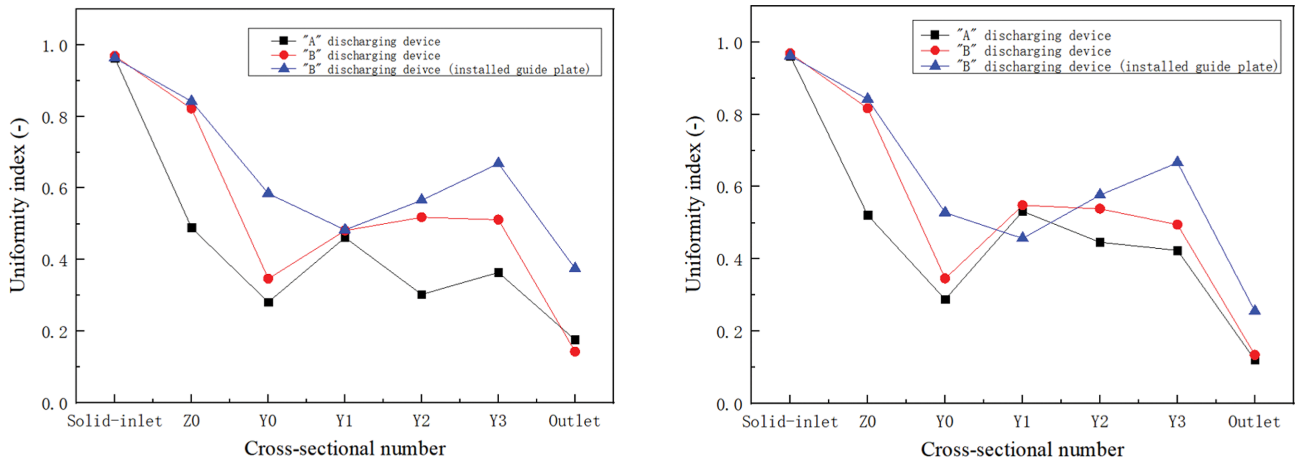

(a) 0.1 kg/s (b) 0.2 kg/s

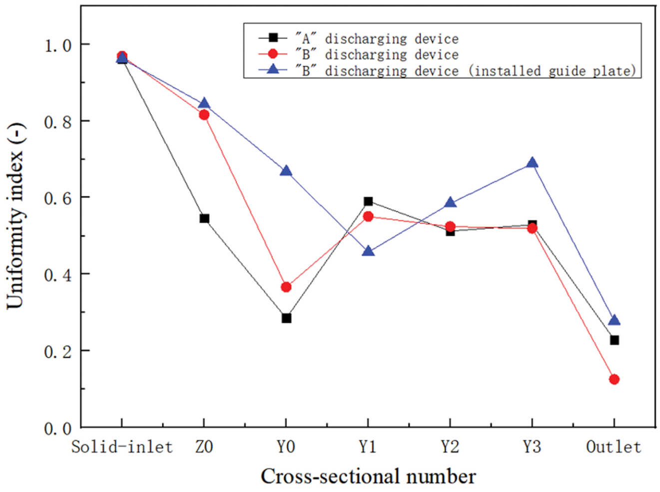

(c) 0.3 kg/s

Fig. 9. Time average uniformity index of the solids content of each cross-section.

Fig. 9 shows the time average uniformity index of particle content of discharging devices at different mass flow rates, which can characterize the distribution state of the particles in the discharging device. The uniformity index (γ_a) represents the variation of the specified variable in the surface, with 1 representing a perfectly uniform distribution, and the smaller the γ_a, the less uniform the distribution, calculated as follows:

$$\gamma_a = 1 - \frac{\sum_{i=1}^{n}[(|\Phi_i - \overline{\Phi_a}|)A_i]}{2|\overline{\Phi_a}|\sum_{i=1}^{n}A_i} \qquad (16)$$

and

$$\overline{\Phi_a} = \frac{\sum_{i=1}^{n}\Phi_i A_i}{\sum_{i=1}^{n}A_i} \qquad (17)$$

It is noteworthy that in the region from Z0 to Y0, the time average uniformity index of particles content of A and B discharging devices decreases significantly. It indicates that the change in the direction of movement of the particles causes a non-uniform distribution, which leads to a greater susceptibility to the collision, accumulation, and even retention of the particles here. The B discharging device (installed guide plate) can improve this problem effectively, which shows that the improved discharging device results in a more uniform flow distribution of particles into the tube after restricting reflux. In addition, the time average uniformity index of particle content at the outlet of the B discharging device (installed guide plate) is significantly higher than that of the two previous discharging devices, but this advantage becomes less pronounced as the solids mass flow rate increases. Therefore, the new improved discharging device has a better enhancement of particle flow uniformity for small flow rates.

We propose the particle retention ratio P_{Tn} to characterize the retention and accumulation of particles occurring in the discharging device. The higher the particle retention ratio, the bigger the proportion of retained particles entering the discharging section during this time period. And severe blockages will occur if the particle retention ratio is too high. Note that the particle retention

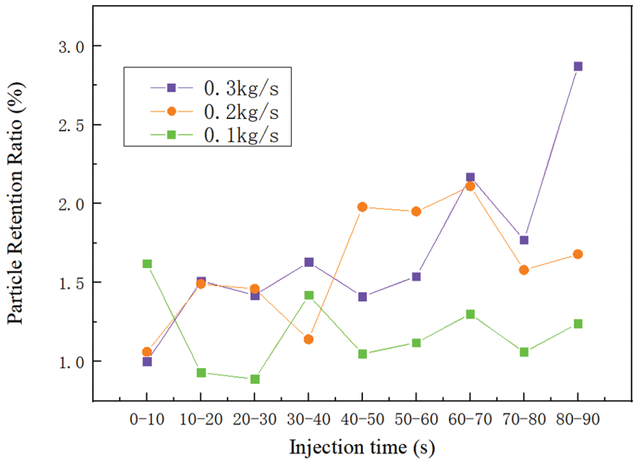

Fig. 10. Particle retention ratio at 100 s of particles entering the B discharging device (installed guide plate) for each time period.

ratio is not the amount of particle retention and the value of the particle retention ratio is much greater than the ratio of the particles that remain in the discharging device to the particles flow through the discharging device. The particle retention ratio is calculated as follows:

$$P_{Tn}=\frac{Q_{tn}}{Q_{Tn100}} \tag{18}$$

where, Tn is the nth interval of 10 s; tn is the time at the end of the Tn time period; Q_{tn} is the number of particles tracked at tn; Q_{Tn100} is the remaining quantity at 100 s of particles that enter the discharging device during the Tn period.

Fig. 10 shows the particle retention ratios at 100 s entering the B discharging device (installed guide plate) at different times period. It can be seen that the higher the mass flow rate, the higher the overall particle retention ratio, with an average particle retention ratio of 1.18%, 1.61%, and 1.70% at 0.1 kg/s, 0.2 kg/s, and 0.3 kg/s, respectively. This is consistent with the phenomena that occurred in experiments. When the mass flow rate of the particles is small, the effect of the gas on the particle population is less obstructive. So at a mass flow rate of 0.1 kg/s, the effect of the gas on the overall particle population is significant and does not cause too many particles to be retained, resulting in a gradual decrease in the particle retention ratio in the early stage and a subsequent stabilization in an acceptable range. The mass flow rate of 0.1 kg/s is also a critical value we are looking for. When the mass flow rate exceeds this equilibrium point, the load on the discharging device increases and the effect of the gas on the particle population is not sufficient to blow out the particles in a continuous large amount, causing some particles to be retained and gradually accumulate, making the particle retention ratio gradually increase at a mass flow rate greater than this. For the particles injected into the discharging device at 0-10 s, the highest particle retention ratio was observed at 0.1 kg/s, which is due to the low total mass of particles and the high retention ratio despite the low retention number. Overall, a mass flow rate of 0.1 kg/s or lower was maintained as much as possible during the operation of the discharging device, which is consistent with the previous findings, which is also consistent with the design in real-life conditions.

During our experiment, we found that the pressure in the storage tank becomes smaller with the discharging operation, and if the gas is not refilled in time, the pressure of the storage tank will be too low to deliver. Therefore, we propose the fluid loss degree to quantify this phenomenon and characterize the degree of fluid loss in the storage tank by the average ratio of fluid mass flow rate at the outlet to the gas mass flow rate at the gas inlet, calculated as Eq. (19). In the experiments, The fluid loss degree was obtained by the mass of gas refilled to the storage tank in 100 s, calculated as Eq. (20).

$$\lambda_n=\frac{\sum_{T=1}^{100}\left(1+\dfrac{Q_i}{Q_s}\right)}{100} \tag{19}$$

where, T is the simulation time, s; Q is the gas volume flow rate, m^3/h; the subscript i and s are the gas phase inlet and outlet of the discharging device, respectively.

$$\lambda_e=1+\frac{Q_c\cdot t\cdot n}{100Q_s} \tag{20}$$

where, t is the length of time for a single gas refill of the storage tank, s; n is the number of refill of the storage tank; Q_c is the volume flow rate of the refill of the storage tank, m^3/h.

Compared to the simulation results with the experimental results, as shown in Fig. 11, overall, both of the simulated and experimental results follow the maximum fluid loss degree of the A discharging device, the minimum fluid loss degree of the B discharging device (installed guide plate). The maximum difference does not exceed 25%. The lower the fluid loss, the greater the driving force for the particles and the ability to maintain continuous transport of the particles. Therefore, it can be considered that the improved B discharging device (installed guide plate) has a better continuous transport capacity. Moreover, for the same discharging device, the gas loss degree obtained in the experiment is higher than the simulated results, which is due to leakage of the equipment during

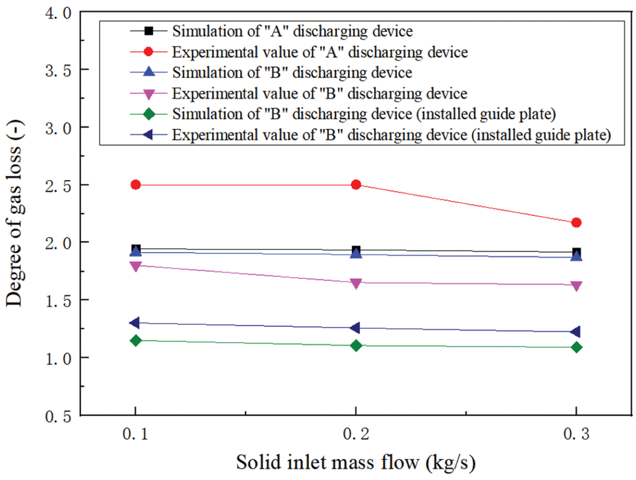

Fig. 11. Fluid loss degree.

the experiment, resulting in uneven gas pressure distribution, and instrumentation measurement errors. Therefore, in practice, care should be taken to check the equipment for air leakage.

CONCLUSION

Based on the development of the continuous production process system of sodium phenol carboxylation reaction, this paper investigated the problem of unstable flow and accumulation of transported fluid and transported particles, then designed, improved and manufactured several pneumatic conveying discharging devices, analyzing and discussing the characteristics of the gas-solid flow field in the discharging device through a combination of numerical simulation and experiment. The main findings are as follows:

(1) The pressure distribution of the CO_2 gas in the B discharging device is more uniform than in the A discharging device, but there is a "reflux chamber" of gas. Both discharging devices A and B had particle accumulation in different areas, making it difficult to achieve a smooth conveying of solid particles.

(2) The B discharging device (installed guide plate) can effectively avoid "blind zones" and "reflux" of the gas in the device, further eliminating the accumulation of particles in the A and B discharging devices, and the time average solid content uniformity index is relatively high in each cross-section, resulting in smoother discharging.

(3) The particle retention ratio was proposed to characterize the particle accumulation phenomenon, and it was found that in the B discharging device (installed guide plate), the higher the mass flow rate, the higher the particle retention ratio, and the advantage of the particle solids uniformity index compared to the A and B discharging devices decreases, so the new discharging device performs better with smaller particle mass flow rate.

(4) The fluid loss degree was proposed to quantify the pressure loss, and the simulation results and experimental results confirmed that the B discharge device (installed guide plate) has the lowest fluid loss degree and better continuous conveying capability.

In summary, the new improved discharging device, i.e., the B discharging device (installed guide plate) is simple in structure and can reduce the particle accumulation and pressure loss problems that tend to occur in conventional bent pipe conveying, and can better support the continuous conveying of sodium phenol, providing a key link for its continuous process development. In addition, since the new discharging device can better replace the role of bent pipe conveying, it can also be adapted to other industrial production where it is difficult to use complex conveying devices due to site constraints, and has a high reference value for applications in fluidized bed systems and similar continuous process transformation. In addition, to have a more systematic and comprehensive understanding of the pneumatic conveying characteristics of the sodium phenol carboxylation continuous production system, we plan to conduct a continuous study of the pneumatic conveying part of the front part of the system (the pellets are transported from the spray drying system to the pellet storage tank section by nitrogen gas), and to investigate the characteristics of the gas-solid two-phase flow field and the effect of the heating device on the wall of the pipe on the secondary drying of the pellets during the process.

ACKNOWLEDGEMENTS

This work was supported by a grant from the Natural Science Foundation of Shandong Province (Grant No. ZR2020MB122), Shandong Province Taishan Scholar engineering under special funding Foundations, and the Tackling Key Program of Science and Technology in Shandong Province (No. 2019GSF109009).

NOTATION

u_x : gas phase velocity in the x direction [m/s]
u_y : gas phase velocity in the y direction [m/s]
F_p : the force of the particle on the fluid [N]
F_x : additional acceleration force [N]
C_C : the Cunningham correction
d_s : particle diameter [mm]
G_k : turbulent kinetic energy
A : circle area [m^2]
P_{Tn} : particle retention ratio
T : simulation time [s]
Q : gas volume flow rate [m^3/h]
Q_c : volume flow rate of the refill of the storage tank [m^3/h]

Greek Letters

α_g : gas phase volume fraction
ρ_g : gas phase density [kg/m^3]
μ_g : fluid shear viscosity [kg/(m·s)]
μ_t : turbulent viscosity [kg/(m·s)]
μ : fluid molecular viscosity [kg/(m·s)]
λ : average free range of gas molecules
μ_x(x=k or ω) : effective viscosity
σ_x(x=k or ω) : diffusion constant of the model
γ_a : uniformity index
Φ : variable for the specified cross-section
$\overline{\Phi}$: average of variables for the specified cross-section

REFERENCES

1. Y. Devani and P. S. Yelamarthi, *J. Food Process. Eng.*, **42**, (2019).
2. G. Strenzke, R. Dürr, A. Bück and E. Tsotsas, *Powder Technol.*, **375**, 210 (2020).
3. Z. Y. Duan, S. J. Sun, Z. J. Lan, Y. Wang, J. M. Zhang and J. T. Wang, *Powder Technol.*, **372**, 428 (2020).
4. D. Geldart, *Powder Technol.*, **7**, 285 (1973).
5. Y. Jin, H. F. Lu, X. L. Guo and X. Gong, *Chem. Eng. Sci.*, **205**, 319 (2019).
6. N. M. Tripathi, N. Santo, A. Levy and H. Kalman, *Powder Technol.*, **345**, 190 (2019).
7. D. Sun, *Powder Technol.*, **390**, 354 (2021).
8. L. M. Gomes and A. L. A. Mesquita, *Chem. Eng. Sci.*, **104**, 780 (2013).
9. S. Matsumoto, M. Kikuta and S. Maeda, *J. Chem. Eng. Jpn.*, **10**, 273 (1977).
10. C. P. Narimatsu and M. C. Ferreira, *Brazil. J. Chem. Eng.*, **18**, 221 (2001).
11. E. Heinl and M. Bohnet, *Chem. Eng. Technol.*, **27**, 1143 (2004).
12. S. Laín and M. Sommerfeld, *Int. J. Multiph. Flow*, **39**, 105 (2012).

13. X. P. Chen, C. L. Fan, C. Liang, W. H. Pu and P. Lu, *Korean J. Chem. Eng.*, **24**, 499 (2007).
14. C. Liang, X. P. Chen, C. S. Zhao, W. H. Pu and P. Lu, *Korean J. Chem. Eng.*, **26**, 867 (2009).
15. B. Liu, Z. D. Wu, G. C. Yin and J. X. Liu, *Mod. Manuf. Eng.*, **03**, 93 (2018).
16. O. Orozovic, A. Lavrinec, Y. Alkassar, J. Chen, K. Williams, M. G. Jones and G. E. Klinzing, *Powder Technol.*, **364**, 218 (2020).
17. Y. F. Wang, Heibei Univ. Technol. (2018).
18. W. P. Hong, B. H. Wang, Y. Liu and H. R. Li, *Powder Technol.*, **375**, 233 (2020).
19. K. Sharma, S. S. Mallick and A. Mittal, *Powder Technol.*, **362**, 707 (2020).
20. Y. Yang, P. Zhang, L. L. He, J. Y. Sun, Z. L. Huang, J. D. Wang and Y. R. Yang, *Chem. Eng. Sci.*, **211**, 115260 (2020).
21. P. Zhang, Y. Yang, Z. L. Huang, J. Y. Sun, Z. W. Liao, J. D. Wang and Y. R. Yang, *Chem. Eng. Sci.*, **229**, 116083 (2020).
22. Y. J. Xiong, X. L. Guo, X. Gong, W. J. Huang, J. C. Zhao and H. F. Lu, *CIESC J.*, **60**, 1421 (2009).
23. J. W. Zhou, X. M. Han, S. X. Jing and Y. Liu, *Chem. Eng. Res. Des.*, **157**, 92 (2020).
24. A. Bansal, S. S. Mallick and P. W. Wypych, *Particul. Sci. Technol.*, **31**, 348 (2013).
25. H. Li and Y. Tomita, *Powder Technol.*, **107**, 144 (2000).
26. H. Holmas, *Chem. Eng. Sci.*, **65**, 1811 (2010).
27. H. Hadziahmetovic, N. Hodzic, D. Kahrimanovic and E. Dzaferovic, *Teh. Vjesn.*, **21**, 275 (2014).